

MIT Open Access Articles

Numerical modeling study to compare the nutrient removal potential of different floating treatment island configurations in a stormwater pond

The MIT Faculty has made this article openly available. **Please share** how this access benefits you. Your story matters.

Citation: Xavier, Manoel Lucas Machado et al. "Numerical modeling study to compare the nutrient removal potential of different floating treatment island configurations in a stormwater pond." *Ecological Engineering* 111 (February 2018): 78-84 © 2017 Elsevier B.V.

As Published: <http://dx.doi.org/10.1016/j.ecoleng.2017.11.022>

Publisher: Elsevier BV

Persistent URL: <https://hdl.handle.net/1721.1/123469>

Version: Author's final manuscript: final author's manuscript post peer review, without publisher's formatting or copy editing

Terms of use: Creative Commons Attribution-NonCommercial-NoDerivs License



1 TITLE: Numerical Modeling Study to Compare the Nutrient Removal Potential of Different Floating
2 Treatment Island Configurations in a Stormwater Pond.

3

4 AUTHORS: Manoel Lucas Machado Xavier^{1,2*}, Johannes Gerson Janzen¹, Heidi Nepf²

5 *corresponding author, mavier89@gmail.com

6 ¹Federal University of Mato Grosso do Sul (UFMS), Campo Grande, MS 79070-900, Brazil

7 ²Department of Civil and Environmental Engineering, Massachusetts Institute of Technology, Cambridge, MA 02139, USA

8

9 ABSTRACT

10 Constructed wetlands, which are commonly used in wastewater treatment, are difficult to use for
11 stormwater treatment, because the water level variation in a stormwater pond makes it difficult for
12 rooted vegetation to survive. As an alternative, vegetation can be grown on floating mats, called floating
13 treatment islands (FTI), with roots extending downward into the water. Nutrient removal is achieved
14 through uptake and trapping by the matrix of roots and bio-film. The overall treatment provided by a
15 pond with FTIs depends on the fraction of flow exposed to the root zone. This study used numerical
16 modeling to study the flow through the root zone, with the goal of determining which configuration of
17 FTI achieved the greatest overall treatment. Six different configurations were considered, all with root
18 zone volume equal to 11% of the pond volume. The permeability of the root zone was estimated using
19 velocity measurements within real floating vegetation. A first-order removal rate within the root zone
20 (k_r) was estimated from removal rates reported in the literature. Preliminary studies considered the
21 similarity in flow and removal between systems of different physical scale. Geometric similarity of the
22 root zone guaranteed flow similarity within the root zone. To achieve performance similarity (same mass
23 reduction), systems need to have the same non-dimensional removal rate ($k_r t_n$, with t_n the nominal
24 residence time of the pond). The consideration of different FTI configurations showed that wakes
25 generated by upstream FTIs lowered the mass removal of downstream FTIs, so that segmenting a single
26 large FTI into multiple smaller FTIs in series did not improve overall nutrient removal. However,
27 segmenting a single FTI into a pair of parallel FTIs did improve the nutrient removal, and this
28 configuration provided the best pond-scale removal.

29

30 HIGHLIGHTS

- 31 • Root zone regions with higher flushing provided greater nutrient removal
- 32 • Breaking a large FTI into smaller FTIs in series did not improve mass removal
- 33 • For FTI arranged in series, wakes produced by upstream FTI reduced the flow entering and the
34 mass removal achieved by downstream FTI
- 35 • For the same total root zone volume, mass removal was highest for a pair of FTI arranged in
36 parallel with the flow.
- 37 • Ponds of different scale but the same geometry and non-dimensional removal rate achieved the
38 same mass removal

39 KEYWORDS: floating treatment islands; stormwater pond; mass removal; numerical modeling

40

41 1. INTRODUCTION

42 Constructed wetlands with rooted plants have been integrated into urban water treatment (Carleton et al., 2001; Crowe et al., 2007; Kadlec and Wallace, 2009; Melbourne Water, 2002), because they have
43 low-maintenance compared to traditional treatment, while also enhancing habitat and providing
44 recreational and aesthetic value to the landscape (Knight et al., 2001; Lee and Li, 2009; Rousseau et al.,
45 2008). This natural infrastructure is difficult to implement for stormwater treatment, because the water
46 level in a stormwater pond varies significantly over time-scales of days and weeks, making it difficult for
47 rooted vegetation to establish and survive (Ewing, 1996; Headley and Tanner, 2006; Greenway and
48 Polson, 2007). Floating treatment islands (FTI) have been introduced as an alternative for stormwater
49 treatment, because the floating vegetation can tolerate large swings in water depth (e.g. Headley and
50 Tanner, 2012). Floating treatment wetlands are an appealing retrofit to existing stormwater ponds,
51 because they do not require additional earthwork or land, and they do not detract from the available
52 storage volume, because they float (Winston et al. 2013).
53

54 A floating treatment island (FTI) consists of emergent vegetation grown hydroponically on a floating
55 mat. The roots grow into the water beneath, providing a large surface area for biofilm growth (Tanner et
56 al 2011). The dangling roots covered with sticky biofilm are very effective in trapping fine particles.
57 Eventually, the particles entrapped in biofilm become heavy enough to slough off and settle to the bed.
58 This entrapment-settling mechanism is the main removal process for particulate-bound nutrients and
59 metals within an FTI (e.g. Hoeger, 1988; Smith and Kalin, 2000; Headley and Tanner 2006; Borne 2014).
60 Some microbial mediation also occurs, but direct uptake by the plants plays a relatively minor role (e.g.
61 Tanner and Headley 2011, Borne 2014, Lane et al. 2016). Several previous studies have compared
62 mesocosms or stormwater ponds with and without FTIs to evaluate the pollutant removal potential. A
63 majority of these studies have shown increased pollutant removal associated with FTIs (e.g. Tanner and
64 Headley, 2012, Lane et al. 2016). For example, Tanner and Headley (2011) showed that FTIs enhanced
65 the removal of copper, phosphorus, and fine suspended sediments. FTIs planted with *Canna flaccida* and
66 *Juncus effusus* deployed in a trough mesocosm removed up to 75% of nitrogen and phosphorus from
67 simulated stormwater (White and Cousins, 2013). Chang et al. (2012) compared ponds with FTIs
68 occupying 5% and 10% of the pond surface area. While both configurations removed nutrients,
69 unexpectedly the removal was similar for 5% and 10% surface coverage. This might be explained by
70 differences in water circulation through the root zone. Indeed, several studies have noted that the
71 treatment provided by individual FTIs depends on the fraction of flow that passes through the root zone,
72 and that an understanding of this process would improve the design of FTIs for applications in rivers and
73 detention ponds (Headley and Tanner, 2012; Chang *et al*, 2012, Pavlineri et al. 2017). The goal of this
74 study was to use Computational Fluid Dynamics (CFD) to study the flow through FTI root zones and to
75 analyze the impact of FTI configuration on the estimated mass removal within individual root zones.
76

77 2. METHODS

78 The stormwater pond geometry was chosen to match the pond described in Khan *et al* (2013), so that
79 Kahn's measurements could be used for model validation. Kahn's experiments were done in a 1:10 scale
80 model of a real stormwater pond located in New Zealand. The model consisted of a rectangular tank
81 with sloping slides (2:1, horizontal:vertical) and top dimensions of length, width and depth equal to 4.1
82 m, 1.5 m, and 0.23 m, respectively. The inlet and outlet pipes had diameters of 45 mm and 105 mm,
83 respectively. The geometry for all FTI configurations is given in Table 1 and shown in Figure 1. For all
84 cases the total root zone volume was 11% of the pond volume.

85
 86
 87
 88
 89
 90
 91
 92
 93
 94
 95
 96
 97
 98
 99
 100
 101
 102
 103
 104
 105
 106
 107
 108
 109
 110

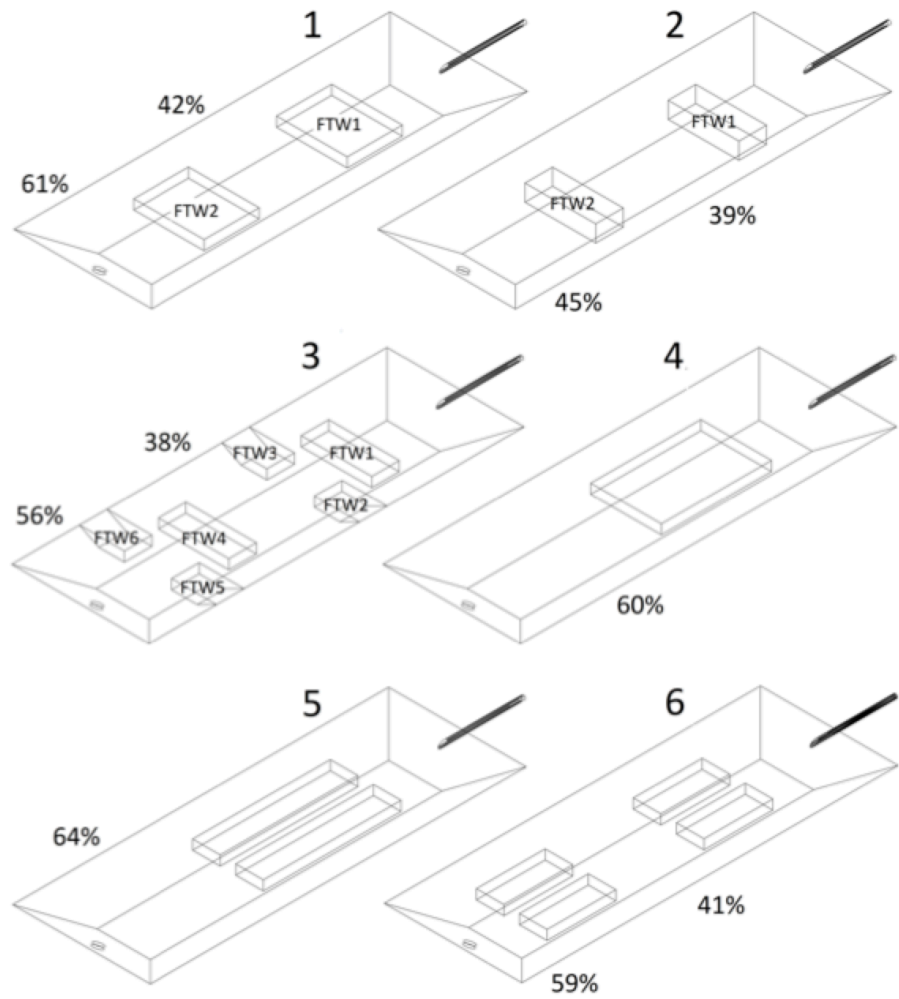


Figure 1: Geometries for the six test cases. Dimensions of individual FTI root zones given in Table 1. The black cylinder represents the inlet pipe. The bold numbers show percent of inject mass removed at the position long the pond corresponding to the number's position. For example, in case 1 the fraction of mass removed between the inlet and the downstream end of FTI1 was 42%, and between the inlet and the outlet was 61%.

Table 1: Dimensions of the root zones (length, width, depth) given in meters.

	FTI1	FTI2	FTI3	FTI4	FTI5 and FTI6
Case 1	0.6, 0.77, 0.105	0.6, 0.77,	---	---	---
Case 2	0.3, 0.8, 0.2	0.3, 0.8, 0.2	---	---	---
Case 3	0.22, 0.77, 0.105	0.3,0.49,0.105	0.3,0.49,0.105	0.3,0.77,0.105	0.3, 0.49, 0.105
Case 4	1.2,0.77,0.105	---	---	---	---
Case 5	1.54, 0.3, 0.105	1.54, 0.3,	---	---	---
Case 6	0.77, 0.3, 0.105	0.77, 0.3,	---	---	---

111

112 The flow field within the pond was determined using the CFD code ANSYS CFX[®] 17.0 with a 3D
 113 transient simulation using the Shear Stress Transport (SST) RANS (Reynolds Averaged Navier-Stokes)
 114 turbulence model. For steady, incompressible flow, the Reynolds-averaged equations for conservation
 115 of mass and momentum are, respectively:

$$116 \quad \frac{\partial u_i}{\partial x_i} = 0 \quad (1)$$

$$117 \quad \rho \frac{\partial u_j u_i}{\partial x_j} = -\frac{\partial p}{\partial x_i} + \mu \frac{\partial^2 u_i}{\partial x_j \partial x_j} - \rho \frac{\partial \overline{u'_i u'_j}}{\partial x_j} + S_{M,i} \quad (2)$$

118 in which i or $j = 1, 2$ or 3 ; x_1, x_2 and x_3 denote the streamwise (x), cross-stream (y), and vertical (z)
 119 directions, respectively; u_1, u_2 and u_3 are the corresponding time-mean velocity components; $\overline{u'_i u'_j}$ is the
 120 Reynolds stress, with u' denoting the fluctuating part of the velocity; p is the pressure; ρ is the fluid
 121 density; μ is the viscosity; and $S_{M,i}$ is a momentum sink used to represent the root zone drag.

122 The turbulent momentum flux was modeled using an eddy viscosity, whose value was predicted
 123 with a k_t - ω method. The specific turbulent kinetic energy, k_t ($m^2 s^{-2}$), and dissipation rate, ω (s^{-1}) were
 124 modeled with the following equations

$$125 \quad \frac{D(\rho k_t)}{Dt} = \frac{\partial}{\partial x_j} \left[(\mu + \sigma_{k2} \mu_t) \frac{\partial k}{\partial x_j} \right] + P_k - \beta^* \rho k \omega \quad (3)$$

$$126 \quad \frac{D(\rho \omega)}{Dt} = \frac{\partial}{\partial x_j} \left[(\mu + \sigma_\omega \mu_t) \frac{\partial \omega}{\partial x_j} \right] + 2(1 - F_1) \rho \sigma_{\omega 2} \frac{1}{\omega} \frac{\partial k_t}{\partial x_j} \frac{\partial \omega}{\partial x_j} + \alpha \rho S^2 - \beta \rho \omega^2 \quad (4)$$

127 in which S is the invariant measure of the strain rate, and the shear production, P_k , was

$$128 \quad P_K = \min \left[\mu_t \frac{\partial u_i}{\partial x_j} \left(\frac{\partial u_i}{\partial x_j} + \frac{\partial u_j}{\partial x_i} \right), 10 \beta^* \rho k_t \omega \right] \quad (5)$$

129 Blending functions F_1 and F_2 were used to smoothly transition from the standard k_t - ω model near the
 130 wall to a k_t - ε model in the outer portion of the boundary layer. The blending function, F_1 was

$$131 \quad F_1 = \tanh(\text{arg}_1^4) \quad (6)$$

$$132 \quad \text{arg}_1 = \min \left[\max \left[\frac{\sqrt{k_t}}{\beta^* \omega d}, \frac{500v}{y^2 \omega} \right], \frac{4\rho\sigma_{\omega 2} k_t}{CD_{k\omega} d^2} \right] \quad (7)$$

$$133 \quad CD_{k\omega} = \max \left(2\rho\sigma_{\omega 2} \frac{1}{\omega} \frac{\partial k_t}{\partial x_j} \frac{\partial \omega}{\partial x_i}, 10^{-10} \right) \quad (8)$$

134 in which d was the distance to the nearest wall. The turbulent eddy viscosity was defined as

$$135 \quad \nu_t = \frac{\mu_t}{\rho} = \frac{\alpha_1 k_t}{\max(a_1 \omega, SF_2)} \quad (9)$$

136 in which F_2 was the blending function

$$137 \quad F_2 = \tanh(\text{arg}_2^2) \quad (10)$$

$$138 \quad \text{arg}_2 = \max \left(\frac{2\sqrt{k_t}}{\beta^* \omega y}, \frac{500v}{y^2 \omega} \right) \quad (11)$$

139 The coefficients of the SST model were: $\beta^* = 0.09$, $a_1 = 0.31$, $\alpha_1 = 0.5532$, $\beta_1 = 0.075$, $\alpha_2 =$
140 0.4403 , $\beta_2 = 0.0828$, $\sigma_{k1} = 1.176$, $\sigma_{k2} = 1$, $\sigma_{\omega1} = 0.5$, $\sigma_{\omega2} = 0.85616$. More details on these
141 coefficients can be found in Menter *et al* (2003). The Second Order Backward Euler Scheme was chosen
142 for the transient scheme.

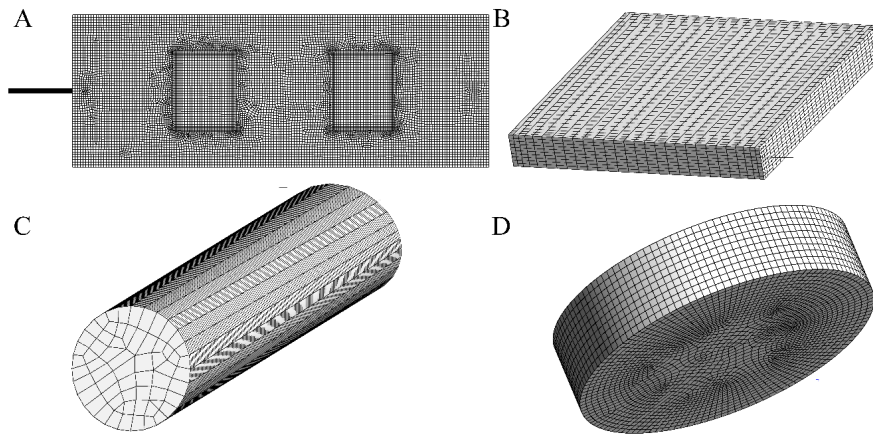
143 The following boundary conditions were defined. A uniform flow was imposed at the inlet. At the
144 outlet, an average static reference pressure of 0 Pa was specified. A no-slip boundary condition was
145 applied at the walls. The free surface was considered a symmetry plane with zero gradient normal to
146 that plane (Stamou 2002). The root zone of each FTI was represented as a porous media using

147
$$S_{M,i} = \frac{\mu}{K_{perm}} u_i \tag{12}$$

148 in which K_{perm} was the permeability. The permeability in the root zone was determined by matching a
149 hydrodynamic simulation to measurements provided in Downing-Kunz and Stacey (2012), who recorded
150 the velocity field within and beneath a root zone of real floating vegetation (*E. crassipes*, water
151 hyacinth). The live vegetation was placed in a 20-m long channel that was 0.6 m wide and filled to a
152 water depth of 0.3 m. Velocity data was extracted from Figure 4 in Downing-Kunz and Stacey (2012), in
153 which the root zone extended 0.62 m in the streamwise direction, and the root depth below surface was
154 0.125m. The floating vegetation filled the channel width. To determine an appropriate permeability for
155 the root zone, the CFD model was configured to represent this channel and run with different values of
156 K_{perm} ranging from 10^{-20} m^2 to 10^{-4} m^2 . The simulated velocity was compared to the velocity profile
157 measured within the root zone, with a good fit observe for $K_{perm} = 10^{-7} \text{ m}^2$. This values was subsequently
158 used in all simulations.

159 The numerical code employed unstructured numerical grids, which permitted a very accurate
160 representation of the boundaries (Figure 2). The grid was created by combining the sweep and the hex
161 dominant methods (ANSYS Inc. 2016b) with finer spacing at the inlet and outlet regions and at the edges
162 of the FTIs. The computational grids for each of the six cases had on the order of 10^5 hexahedral
163 elements. More details of the governing equations, turbulence model, and algorithms can be found in
164 the CFX® user’s guide (ANSYS Inc. 2016a).

165
166



167
168 **Figure 2:** Examples of the mesh for components of the numerical pond model in Case 1: (A) the pond with two
169 FTIs; (B) close up of one FTI; (C) inlet pipe; and (D) outlet pipe.

170

171 The evolution of the concentration field, C , was described using conservation of mass,

$$172 \quad \frac{\partial C}{\partial t} + \frac{\partial(u_i C)}{\partial x_i} = \frac{\partial}{\partial x_i} \left(\frac{v_t}{Sc} \frac{\partial C}{\partial x_i} \right) - k_r C \quad (13)$$

173 with turbulent Schmidt number, $Sc = (v_t / D_t)$, set to 1, which falls within the range of measured
 174 values, with D_t the turbulent diffusivity (e.g. Gualtieri et al. 2017). Removal within the root zones was
 175 represented by a first-order reaction ($k_r C$), and this term was set to zero outside the root zones. The
 176 water surface and all solid surfaces were modeled with a no-flux boundary condition. Realistic values for
 177 the first-order rate constant k_r were inferred from mesocosm studies that reported removal rate
 178 constants (k_v) for the entire mesocosm volume (V_m). Assuming that mixing through the root zone was
 179 not limiting and that removal only occurred within the root zone volume (V_{root}), the rate constant within
 180 the root zone (k_r) can be estimated as $k_r = k_v(V_m/V_{root})$. Values extracted from the literature are reported
 181 in Table 2.

182

183 **Table 2:** Root-zone removal rates for total nitrogen estimated from measured removal within mesocosm

Author	Vegetation	V_m/V_{root}	k_v (day ⁻¹)	k_r (day ⁻¹)
Chang et al (2012)	<i>Juncus Edgariae</i>	5.36	0.09	0.43
Chua et al (2012)	<i>Carex Virgata</i>	1.75	0.73	1.28
Chua et al (2012)	<i>Shoenoplectus tabernaemontani</i>	1.61	0.73	1.18
Chua et al (2012)	<i>Cyperus ustulatus</i>	1.47	0.73	1.07
Chua et al (2012)	<i>Juncus edgariae</i>	1.15	0.73	0.84

184

185 The simulation was validated using the physical experiments of Khan et al. (2013). Specifically, we
 186 used Case 12 in Khan, which corresponded to Case 1 in Figure 3. Khan characterized the pond circulation
 187 using the residence time distribution (RTD) determined from a standard tracer study. Tracer is
 188 introduced at the inlet as a single slug of mass, M , and the water concentration at the outlet, C_e , is
 189 recorded as a function of time, t . The RTD is then (e.g. Werner and Kadlec, 1996)

$$190 \quad RTD(t) = \frac{QC_e(t)}{\int_0^\infty QC_e(t)dt} \quad (14)$$

191 Q is the pond inflow/outflow rate. The mean residence time, t_{mean} , is the first moment of the RTD, and
 192 the nominal residence time is

$$193 \quad t_n = \frac{V}{Q}, \quad (15)$$

194 with V the system volume.

195 A numerical tracer study was conducted to determine the simulated RTD, which was then validated
 196 against the measured RTD provided in Khan et al (2013). To represent a conservative tracer in the
 197 simulation, the removal term in (13) was set to zero ($k_r=0$) everywhere in the domain. The simulations
 198 was set up to match the conditions in Khan et al. (2013), with flow rate $Q = 1$ L/s and mass $M = 0.01$ g
 199 injected at the inlet. This was recreated in the CFD model with a 1s injection in the inlet pipe, 720 mm
 200 upstream of the pond. The tracer concentration was monitored at the outlet to produce the RTD curve
 201 following equation 14. The simulation was run until 95% of the tracer exited the pond. The simulation

202 was carried out using a time step that varied between 0.1 and 1 s. A smaller time step was used for the
203 time intervals in which there was a higher variation of concentration (e.g., the tracer injection period).
204 These time steps were chosen after a series of tests with decreasing time step showed that decreasing
205 the time step further had no influence on the result.

206 After validation of the numerical model, additional simulations were run to explore different FTI
207 configurations (Figure 3). The removal performance of each configuration was compared using a
208 reactive tracer study, i.e. with the removal term active in equation 13. Mass M was instantaneously
209 injected at the inlet, and the exit concentration, $C_e(t)$, was recorded. The mass escaping the pond, M_e ,
210 was then,

$$211 \quad M_e = \int Q C_e dt \quad (16)$$

212 The fractional removal was defined as the ratio of mass escaping to mass injected,

$$213 \quad \%M_e = \frac{M_e}{M} \quad (17)$$

214 Note that this metric is equivalent to the more common performance metric based on the steady-state
215 outlet concentration, C_e , given a steady-state inflow concentration of C_o , i.e. steady state $C_e/C_o = \%M_e$.
216 In some cases, it was more convenient to consider the fraction of mass removed, which is simply

$$217 \quad \%M_{removed} = (1 - \%M_e) \quad (18)$$

218 To assess the relative contributions of different FTIs within a pond, multiple simulations were run
219 with the removal term ($k_r C$) turned on only for selected root zones. For example, in Cases 1 through 4,
220 the removal achieved by the first FTI in series was calculated by running the tracer simulation with
221 removal turned on only within the first FTI (or first set of three FTIs in case 3). To assess the
222 performance of individual FTI in series, it was necessary to account for the mass removed by upstream
223 FTI. For this reason, the following removal efficiency was defined for an individual FTI,

$$224 \quad \%M_{FTI} = \frac{(M_{in} - M_{out})}{M_{in}} \quad (19)$$

225 in which M_{in} and M_{out} are defined as the mass passing the cross-section directly upstream and
226 downstream, respectively, of the FTI. Finally, to illustrate the flow within individual root zones, an bulk
227 streamwise velocity within the root zone (U_{root}) was calculated by averaging over vertical slices (y - z
228 plane) within the root zone and at different distances (x) from the leading edge of the root zone. The
229 value of U_{root} at the leading edge of the root zone was denoted as U_o .

230

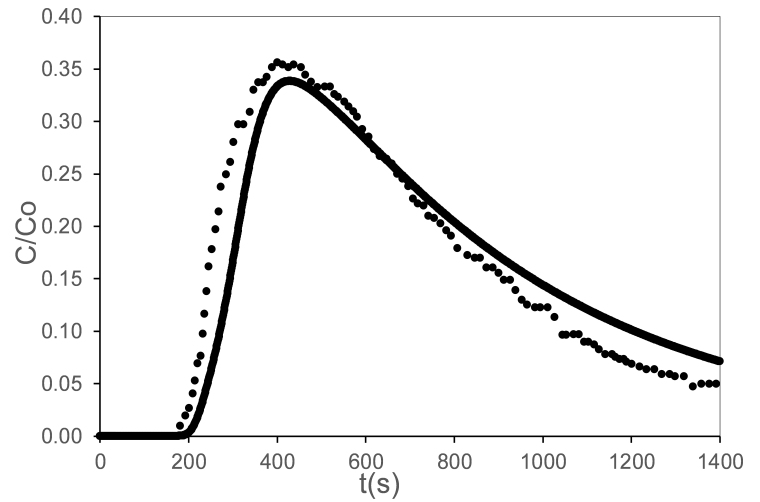
231 3. RESULTS AND DISCUSSION

232

233 3.1. Model Validation

234 The numerical model predicted the measured RTD with good agreement, as shown in Figure 2. The
235 simulated mean residence time, $t_{mean} = 721.5$ s, was nearly identical to the experimental value of 721.7 s.
236 The peak arrival time was also nearly identical at 400.6 s and 408.6 s for the experiment and CFD,
237 respectively.

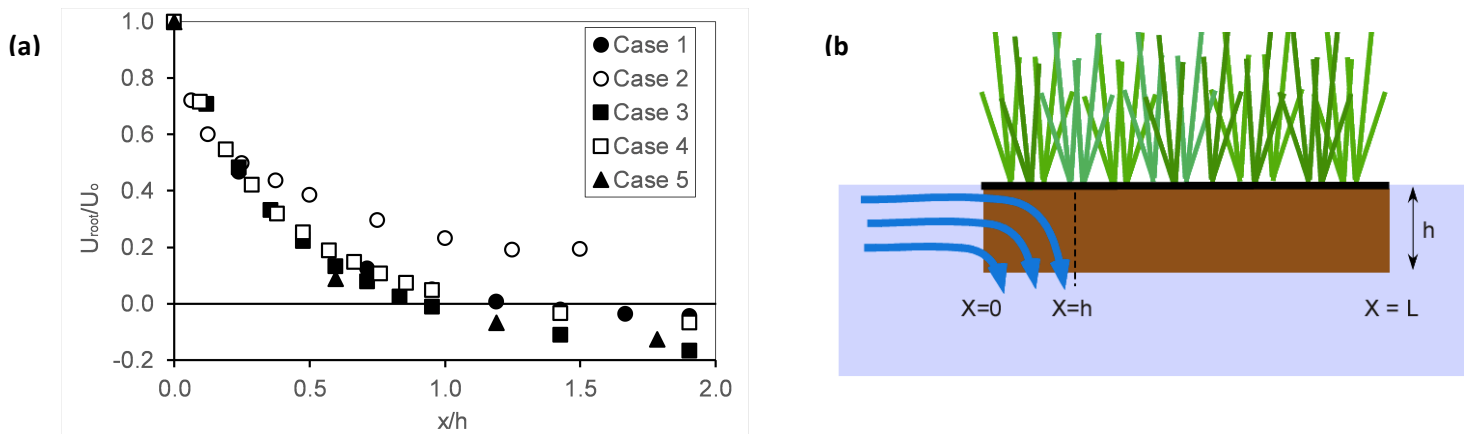
238 **Figure 3:** Comparison between simulated (solid line)
 239 and experimental (dots) tracer concentration at the
 240 outlet, C , normalized by $C_0 = M/V$ for Case 12 in
 241 Khan et al. (2013). For a constant flow rate, Q , which
 242 is valid here, the curve is a surrogate for the RTD .



243
 244
 245

246 3.2. Flow and Performance Similarity

247 To relate simulation results to real systems at different physical scale, we must understand the similarity
 248 between systems of different scale. If the Reynolds number is high enough (> 2000) to ensure inertia-
 249 dominated flow at the pond-scale, which is true for all cases considered here, the pond-scale circulation
 250 pattern will be similar between systems of different physical scale, once normalized by the inflow
 251 velocity. However, flow within the root zone is drag-dominated, so we cannot appeal to Reynolds
 252 number similarity. Flow entering a porous layer is decelerated by the high drag within the layer over
 253 length X_D . As flow decelerates within the layer, conservation of mass requires that some flow be
 254 deflected out of the layer. For a layer with high root density, called high flow blockage, X_D is set by the
 255 cross-stream dimension of the porous layer (Rominger and Nepf 2011, Chen et al. 2013). In this study
 256 the root zone has two cross-stream dimensions (width, w , and depth h), so that $X_D \sim \min(h, w)$.
 257 Assuming the root zones represent high-flow blockage regimes, the ratio X_D/h (or X_D/w) will be the same
 258 for any scale of geometrically-similar root zone. The high-flow blockage scaling was confirmed through
 259 simulation. For each root zone, the streamwise velocity within the root zone, U_{root} , decreased with
 260 increasing distance from the leading edge (Figure 4a). As the streamwise velocity within the root zone
 261 decreased, flow exited the root zone predominantly through the bottom interface (Figure 4b). In all
 262 cases, with different values of h (Table 1), the flow decreased to zero, or reached a constant value at
 263 $x/h \approx 1$, indicating that the adjustment length was set by the root depth, $X_D = h$.

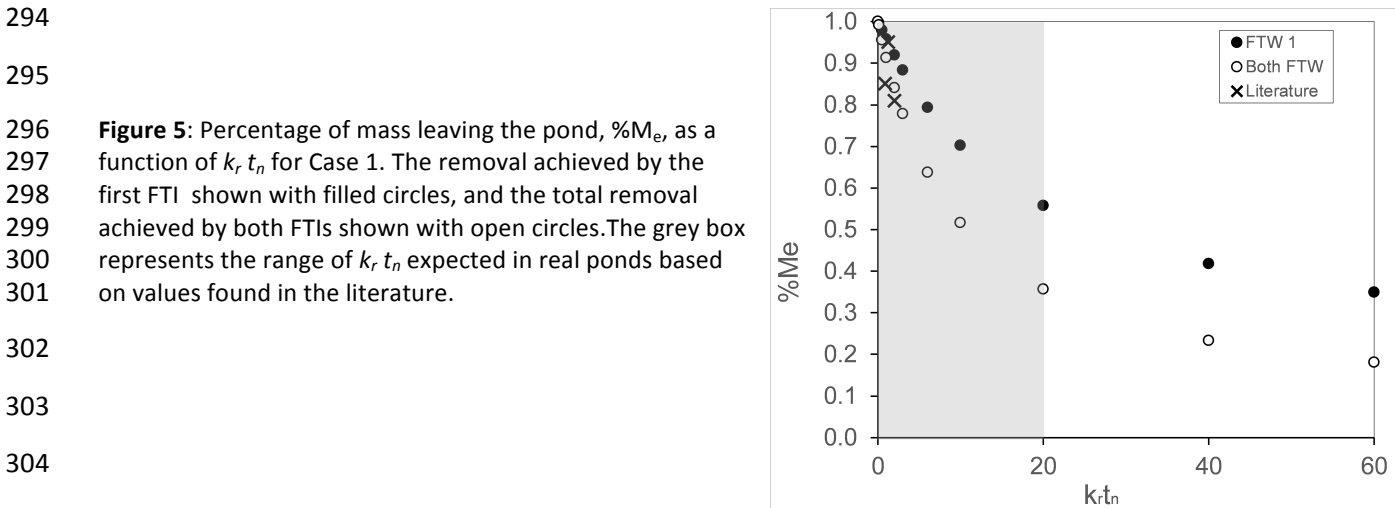


264

265 **Figure 4:** (a) Root-zone-average velocity, U_{root} , normalized by average velocity at the root-zone leading edge, U_0 ,
 266 as a function of distance from leading edge of the root zone (x) normalized by the root depth (h). Data shown for
 267 the most upstream FTI in cases 1 to 5. (b) Schematic of flow entering leading edge of root zone. Flow decelerates
 268 upon entering root zone, and is deflected out of root zone over distance $X_D = h$.

269 To confirm the flow similarity across physical scale, we ran an additional simulation for a full-scale
 270 version of Case 1, with dimensions of 41m, 15m and 2.3m for length, width and depth respectively, as
 271 reported in Khan et al (2013). The geometry of the velocity vectors was nearly identical in the lab- and
 272 full-scale simulations, both in the open regions of the flow and within the root zones. Specifically, the
 273 length-scale of flow deceleration in the root zone was $X_D/h = 1.2 \pm 0.1$ and 1.3 ± 0.1 in the lab- and full-
 274 scale simulations, respectively. We also confirmed that flow similarity ensured performance similarity.
 275 The pond removal was calculated at both scales using tracer simulations with the same non-dimensional
 276 root zone removal rate, $k_r t_n = 60$. The lab-scale and full-scale simulations yielded nearly identical
 277 performance, $\%M_e = 15$ and 14% , respectively. The similarity in mass removal for the lab- and field-scale
 278 simulation confirmed that the appropriate removal rate to achieve similarity between systems of
 279 different physical scale is determined by the non-dimensional removal rate ($k_r t_n$). That is, to produce
 280 the same mass removal in geometrically similar systems of different physical scale (and different t_n) one
 281 must match the non-dimensional removal rate (same $k_r t_n$). Using this similarity, one can predict the
 282 performance of geometrically similar ponds at different physical scale.

283 Using Case 1 as an example, the fraction of mass leaving the pond, $\%M_e$, decreased with increasing
 284 non-dimensional removal rate (Figure 5). For comparison, this figure shows both the removal achieved
 285 by the first FTI (filled circles) and the total removal achieved by both FTIs (open circles). For this
 286 configuration, FTI1 provided more mass removal than FTI2, with FTI1 achieving 60 to 70% of the total
 287 mass removal at each condition. Because we have confirmed flow similarity at the pond-scale and root-
 288 scale, Figure 5 can be used to infer the performance of systems of different physical scale. Field-scale
 289 residence times reported in the literature range from 1 to 16 days (summarized in Headley and Tanner
 290 2012). Combining with the estimated k_r values (Table 2), full-scale ponds fall into the range of
 291 normalized removal rates of $k_r t_n = 0.43$ to 20 . The grey box in Figure 5 marks this range. From this
 292 analysis, we infer that the configuration in case 1 could provide between 5% ($t_n = 1$ day) and 65% ($t_n = 16$
 293 day) mass removal at the field scale.



296 **Figure 5:** Percentage of mass leaving the pond, $\%M_e$, as a
 297 function of $k_r t_n$ for Case 1. The removal achieved by the
 298 first FTI shown with filled circles, and the total removal
 299 achieved by both FTIs shown with open circles. The grey box
 300 represents the range of $k_r t_n$ expected in real ponds based
 301 on values found in the literature.

302
 303
 304
 305

306 At high values of $k_r t_n$ all mass entering a root zone will be removed, so that the overall mass
 307 removal achieved by the pond will be limited by the fraction of mass that passes through the root zone.
 308 To demonstrate this, consider just the removal by FTI1 (black circles in Figure 5). The inflow into FTI1
 309 occurred mainly through the front face, so that the mass entering FTI1 can be estimated by integrating
 310 uC over the front face and over time $[\iint uC dA dt]$. This indicated that 69% of mass entering the pond
 311 entered the root zone of FTI1. The maximum pond-scale removal would occur if all mass entering the

312 root zone were taken up, which, if only FTI1 were active, would produce $\%M_e = 0.31$. This a reasonable
313 fit for the asymptote for FTI1 (black symbols in Figure 5). It is important to note that the position of the
314 inflow jet relative to FTI1 (Figure 1) drives this high fraction of inflow mass into the root zone. In
315 contrast, less mass enters the root zone if the approaching flow is uniform channel flow. Specifically,
316 consider the flow conditions studied by Downing-Kunz and Stacey (2012), in which upstream flow
317 approached the root zone as a uniformly distributed channel flow. Simulations with this configuration
318 showed that only 30% of the mass approaching the root zone entered the root zone, so that less
319 removal would be expected with this configuration. This comparison illustrated an important design
320 element. Positioning the first FTI close to a concentrated inflow jet enhanced mass flux into the root
321 zone, which would likely enhance mass removal.

322

323 3.3. Comparison of FTI Configurations

324

325 3.3.1. Single FTI and FTI in Series

326 When FTI were positioned in series, the mass reduction achieved by the first FTI was always greater than
327 that achieved by the second FTI. For example, in case 1 FTI1 removed 42% of the inlet mass, and FTI2
328 removed just 19% (Figure 5). The lower mass removal achieved in the downstream FTI was due in part
329 to the first-order reaction, *i.e.* because the downstream FTI received less mass, it also removed less
330 mass. To examine the FTI specific removal, $\%M_{FTI}$ considers the mass removed normalized by the mass
331 arriving at a specific FTI (see eq. 19 in Methods), which corrected for the fact that downstream FTI were
332 exposed to lower concentration. However, even with this correction, the downstream FTI removed a
333 smaller fraction of the mass it received, compared to the first FTI in series (Table 3). The lower mass
334 removal in the downstream FTI was correlated with a lower fraction of inflow entering the downstream
335 FTI (Figure 6, black dots). That is, if less flow entered the FTI, less removal occurred. The downstream
336 FTIs removed less mass because they were located in the wakes of the upstream FTI, which diminished
337 the velocity approaching the downstream FTI, which in turn diminished the flow entering the
338 downstream FTI (Table 3). The conclusion drawn from this series of cases (Table 3) was that breaking a
339 single large FTI into smaller FTIs in series did not improve the mass removal, because the upstream FTI
340 created wakes that diminished the performance of the downstream FTI. If FTI were to be implemented
341 in series, the downstream FTI should be spaced far enough apart to avoid wakes of upstream FTI.

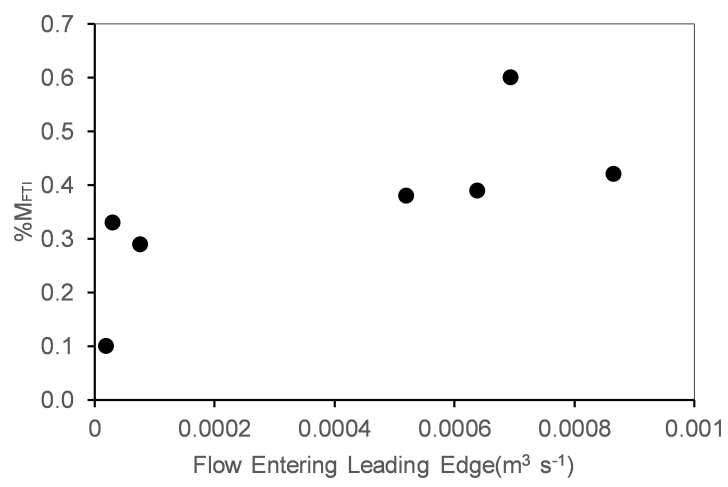
342

343

344 **Figure 6.** Individual FTI removal efficiency, $\%M_{FTI}$,
345 increased as the flow entering the leading edge of
346 the root zone increased. Data from Cases 1 to 4.

347

348



349 **Table 3:** Flow rate entering and mass removal
 350 achieved by individual FTI

Case	%M _{FTI} eq. 19	Flow rate entering FTI (m ³ s ⁻¹)
1 - FTI 1	0.42	8.7 E-04
1 - FTI 2	0.33	3.1 E-05
2 - FTI 1	0.39	6.4 E-04
2 - FTI 2	0.10	2.0 E-05
3 - FTI set 1	0.38	5.2 E-04
3 - FTI set 2	0.29	7.7 E-05
4	0.60	6.9 E-04

351
 352
 353
 354
 355

356

357

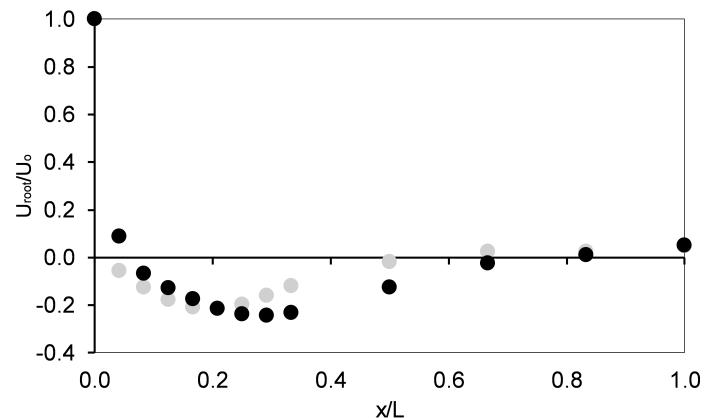
358 **3.3.2. FTI in Parallel**

359 Case 5 produced the highest removal (64% removal). Cases 5 and 6 were distinct in that the islands were
 360 laid out in parallel, not in series. The inlet jet entered the FTI region through the space in between the
 361 two FTIs. Considering Case 5 with two FTI in parallel, the streamwise flow measured within the root
 362 zones showed three distinct regions. First, flow entering the leading edge decelerated over distance $X_D \approx$
 363 $h = 0.105$ m, corresponding to $x/L = 0.07$ (Figure 7). Over this distance all of the flow entering the
 364 leading edge was deflected out of the root zone, so that the flow in the root zone reached zero at X_D .
 365 Immediately downstream of this, the flow in the root zone was reversed (moving upstream) over the
 366 distance $x/L = 0.07$ to 0.6. Rominger and Nepf (2011) also observed flow reversal within high flow-
 367 blockage porous layers and attributed it to the adverse pressure gradient developed at the leading edge.
 368 In the present case, elevated velocity generated between the two root zones at the leading edge
 369 produced a local low-pressure, creating a reversed pressure gradient within the root zone. Because flow
 370 inertia within the root zone was low, the flow reversed in response to this locally adverse pressure
 371 gradient. This is similar to the flow separation and recirculation generated by local adverse pressure
 372 gradients developed around solid obstructions. This phenomenon has also been observed near the
 373 leading edge of dense terrestrial canopies (Krzikalla, 2005). Finally, at the trailing edge of the root zone
 374 ($x/L = 0.6$ to 1) the flow was again in the positive direction, but of relatively small magnitude, compared
 375 to the region of flow reversal.

376 The removal achieved by each velocity zone was estimated by progressively turning on the first-
 377 order reaction in the tracer simulation ($k_r C$ in eq. 13). The region of reversed flow provided the most
 378 removal (36% of injected mass), compared to just (10%) and (18%) within the leading and trailing edges,
 379 respectively. That is, the highest removal was achieved in the zone with the highest flow (Figure 7).
 380 Consistent with Figure 6, this again indicated that the removal within the root zone was controlled by
 381 the supply of water into the root zone, with the highest removal achieved in the regions with greatest
 382 flushing. Finally, case 6 explored the combination of FTI in parallel and in series. The removal for this
 383 case was smaller than case 5, consistent with the conclusions drawn in section 2.1. Specifically, splitting
 384 a single larger FTI into smaller islands in series
 385 did not improve removal.

386

387 **Figure 7:** Streamwise distribution of streamwise
 388 velocity through the root zone, U_{root} , normalized by
 389 the velocity at the leading edge, U_o , for case 5. The
 390 right and left-hand FTI depicted with black and gray
 391 symbols, respectively.



392 4. CONCLUSIONS

393 This study used numerical simulation to study the factors controlling flow and mass removal in
394 detention ponds with floating treatment islands. In these systems, the basin-scale flow is inertia
395 dominated, but the root-zone flow is drag dominated. The flow distribution in a root zone is determined
396 by root zone geometry, such that geometric similarity between systems ensures similarity in root zone
397 flow. Further, to achieve performance similarity (same mass reduction) two systems must have the
398 same non-dimensional root zone removal rate ($k_r t_n$). These scaling rules were confirmed through a
399 comparison of flow and mass reduction between geometrically similar systems at different physical
400 scale.

401 A study of six different FTI configurations of equal total root volume revealed the following concepts
402 that can inform the better design of future FTI applications. First, through all configurations, higher
403 removal was achieved by the FTI or portion of FTI with the highest flow rate within the root zone. This
404 confirmed that the removal achieved by FTI is controlled by the magnitude of flow through the root
405 zone, as previously suggested Headley and Tanner (2012). Second, the segmentation of a single large FTI
406 into multiple smaller FTI arranged in series reduced the pond-scale removal. This trend arose because
407 the wakes generated by upstream FTIs reduced the flow impinging on the downstream FTIs, which
408 reduced the flow passing into the downstream root zones, which in turn reduced the removal achieved
409 by the downstream FTIs. If FTIs are to be implemented in series, the downstream FTI should be spaced
410 far enough away to avoid wakes of upstream FTI. Finally, parallel arrangements of FTI provided greater
411 mass removal than single FTI or FTI in series, with the greatest mass removal achieved by a single pair of
412 FTI configured in parallel.

413

414 ACKNOWLEDGMENTS - This research was funded by a seed grant from the MIT Abdul Latif
415 Jameel World Water and Food Security Lab.

416

417

418 REFERENCES

- 419 ANSYS Inc., 2016a. CFX-Pre Users Guide Release 17.0.
420 ANSYS Inc., 2016b. Meshing Users Guide Release 17.0.
421 Borne, K.E. 2014. Floating treatment wetland influences on the fate and removal performance of phosphorus in
422 stormwater retention ponds. *Ecol. Eng.*, 69, 76–82.
423 Carleton, J., T. Grizzard, A. Godrej, and H. Post. 2001. Factors affecting the performance of stormwater treatment
424 wetlands. *Water Research*, 35, 1552–1562.
425 Chang, N., K. Islam, Z. Marimon, and M. Wanielista. 2012. Assessing biological and chemical signatures related to
426 nutrient removal by floating islands in stormwater mesocosms. *Chemosphere*, 88:736-743.
427 Chen, Z., C. Jiang, and H. Nepf. 2013. Flow adjustment at the leading edge of a submerged aquatic canopy. *Water*
428 *Res. Res*, doi:10.1002/wrcr.20403.
429 Chua, L., S. Tan, C. Sim, and M. Goyal. 2012. Treatment of baseflow from an urban catchment by a floating wetland
430 system. *Ecological Engineering*, 49:170-180.
431 Crowe, A., Q. Rochfort, K. Exall and J. Marsalek. 2007. Controlling urban stormwater by constructed wetlands: A
432 Canadian perspective. *International Journal of Water*, 3:214–230.
433 Downing-Kunz, M., and M. Stacey. 2012. Observations of mean and turbulent flow structure in a free-floating
434 macrophyte root canopy. *Limn. Ocean.: Fluids and Environments*, 2:67-79
435 Ewing, K.. 1996. Tolerance of four wetland plant species to flooding and sediment deposition. *Environ. Exp. Bot.*,
436 36:131–146.
437 Greenway, M., C. Polson. 2007. Macrophyte establishment in stormwater wetlands: coping with flash flooding and
438 fluctuating water levels in the subtropics. In: Proceedings from World Water and Environmental Congress,
439 Tampa, Florida.
440 Headley, T., and C. Tanner. 2006. Application of Floating Wetlands for Enhanced Stormwater Treatment: A Review.
441 NIWA Client Report, Auckland Regional Council, New Zealand.
442 Headley, T., and C. Tanner. 2012. Constructed wetlands with floating emergent macrophytes: an innovative
443 stormwater treatment technology. *Crit. Rev. Environ. Sci. Technol.* 42, 2261e2310.
444 Hoeger, S. 1988. Schwimmkampen: Germany's artificial floating islands. *J. Soil Water Conserv*, 43, 304–306.
445 Kadlec, R., and S. Wallace. 2009. *Treatment Wetlands* (2nd ed.). Boca Raton, FL: CRC Press.
446 Khan, S., B. Melville, and A. Shamseldin. 2013. Design of storm-water retention ponds with floating treatment
447 wetlands. *J.Environmental Engineering*, 139(11):1343-1349.
448 Knight, R., R. Clarke, and R. Bastian. 2001. Surface flow (SF) treatment wetlands as a habitat for wildlife and
449 humans. *Water Science and Technology*, 44:27–37.
450 Krzikalla, F.. 2005. Numerical investigation of the interaction between wind and forest and heterogeneous
451 conditions. Master's Thesis, University of Karlsruhe.
452 Lane, S., D. Sample, A. Lazur, R. Winston, C. Streb, D. Ferrier, L. Linker and K. Brittingham, 2016, Recommendations
453 of the Expert Panel to Define Removal Rates for Floating Treatment Wetlands in Existing Wet Ponds,
454 Chesapeake Research Consortium, [http://chesapeakestormwater.net/bmp-resources/floating-](http://chesapeakestormwater.net/bmp-resources/floating-treatment-wetlands/)
455 [treatment-wetlands/](http://chesapeakestormwater.net/bmp-resources/floating-treatment-wetlands/)
456 Lee, J., and M.-H. Li. 2009. The impact of detention basin design on residential property value: case studies using
457 GIS in the hedonic price modeling. *Landscape and Urban Planning*, 89:7–16.
458 Melbourne Water. 2002. *Constructed wetland systems: Design guidelines for developers*. Melbourne, Australia:
459 Melbourne Water.
460 Menter, F. R., Kuntz, M., and Langtry, R. 2003. Ten years of industrial experience with the SST turbulence
461 model. *Turbulence, heat and mass transfer*, 4(1), 625-632.
462 Pavlineri N., N. Skoulikidis, A. Vassilios, A. Tsihrintzis. 2017. Constructed Floating Wetlands: A review of research,
463 design, operation and management aspects, and data meta-analysis. *Chemical Engineering Journal* 308: 1120–
464 1132
465 Rominger, J., and H. Nepf. 2011. Flow adjustment and interior flow associated with a rectangular porous
466 obstruction. *J. Fluid. Mech.*, 680:636–659, doi:10.1017/jfm.2011.199
467 Rousseau, D., E. Lesage, A. Story, P. Vanrolleghem, and N. De Pauw. 2008. Constructed wetlands for water
468 reclamation. *Desalination*, 218:181–189.

469 Smith, M., and M. Kalin, 2000. Floating wetland vegetation covers for suspended solids removal. Proceedings of
470 the Quebec 2000: Millennium Wetland Event. Quebec City, Quebec: 244.
471

472 Stamou, A.. 2002. Verification and application of a mathematical model for the assessment of the effect of guiding
473 walls on the hydraulic efficiency of chlorination tanks. *J. Hydroinformatics*, 4(4):245-254.

474 Tanner, C., and T. Headley. 2011. Components of floating emergent macrophyte treatment wetlands influencing
475 removal of stormwater pollutants. *Ecological Engineering*, 37(3):474-486.

476 Werner T., R. Kadlec. 1996. Application of residence time distributions to stormwater treatment systems.
477 *Ecological Engineering*, 7(3): 213-234.

478 White, S. and, M. Cousins. 2013. Floating treatment wetland aided remediation of nitrogen and phosphorus from
479 simulated stormwater runoff. *Ecological Engineering*, 61, 207-215.

480 Winston, R., W. Hunt, S. Kennedy, L. Merriman, J. Chandler, and D. Brown, 2013. Evaluation of floating treatment
481 wetlands as retrofits to existing stormwater retention ponds. *Ecological Engineering*, 54: 254-265,
482 <http://linkinghub.elsevier.com/retrieve/pii/S0925857413000384>.
483